Title

Differential pathlength factor informs evoked stimulus response in a mouse model of Alzheimer's disease

Journal

Neurophotonics, 2(4)

ISSN

2329-423X

Authors

Lin, Alexander J

Ponticorvo, Adrien

Durkin, Anthony J

et al.

Publication Date

2015-10-12

DOI

10.1117/1.nph.2.4.045001

Peer reviewed

Neurophotonics

Neurophotonics.SPIEDigitalLibrary.org

Differential pathlength factor informs evoked stimulus response in a mouse model of Alzheimer's disease

Alexander J. Lin
Adrien Ponticorvo
Anthony J. Durkin
Vasan Venugopalan
Bernard Choi
Bruce J. Tromberg

SPIE.

Neurophotonics 2(4), 045001 (Oct–Dec 2015)

Differential pathlength factor informs evoked stimulus response in a mouse model of Alzheimer's disease

Alexander J. Lin,[a,b] Adrien Ponticorvo,[a] Anthony J. Durkin,[a] Vasan Venugopalan,[a,c] Bernard Choi,[a,b,d] and Bruce J. Tromberg[a,b,*]

[a]University of California, Irvine, Beckman Laser Institute and Medical Clinic, 1002 Health Sciences Road, Irvine, California 92612, United States
[b]University of California, Irvine, Department of Biomedical Engineering, 3120 Natural Sciences II, Irvine, California 92697-2715, United States
[c]University of California, Irvine, Department of Chemical Engineering and Materials Science, 916 Engineering Tower, Irvine, California 92697-2575, United States
[d]University of California, Irvine, Edwards Lifesciences Center for Advanced Cardiovascular Technology, 2400 Engineering Hall, Irvine, California 92697-2730, United States

Abstract. Baseline optical properties are typically assumed in calculating the differential pathlength factor (DPF) of mouse brains, a value used in the modified Beer–Lambert law to characterize an evoked stimulus response. We used spatial frequency domain imaging to measure *in vivo* baseline optical properties in 20-month-old control ($n = 8$) and triple transgenic APP/PS1/tau (3xTg-AD) ($n = 5$) mouse brains. Average μ_a for control and 3xTg-AD mice was 0.82 ± 0.05 and 0.65 ± 0.05 mm^{-1}, respectively, at 460 nm; and 0.71 ± 0.04 and 0.55 ± 0.04 mm^{-1}, respectively, at 530 nm. Average μ_s' for control and 3xTg-AD mice was 1.5 ± 0.1 and 1.7 ± 0.1 mm^{-1}, respectively, at 460 nm; and 1.3 ± 0.1 and 1.5 ± 0.1 mm^{-1}, respectively, at 530 nm. The calculated DPF for control and 3xTg-AD mice was 0.58 ± 0.04 and 0.64 ± 0.04 OD mm, respectively, at 460 nm; and 0.66 ± 0.03 and 0.73 ± 0.05 OD mm, respectively, at 530 nm. In hindpaw stimulation experiments, the hemodynamic increase in brain tissue concentration of oxyhemoglobin was threefold larger and two times longer in the control mice compared to 3xTg-AD mice. Furthermore, the washout of deoxyhemoglobin from increased brain perfusion was seven times larger in controls compared to 3xTg-AD mice ($p < 0.05$). [DOI: 10.1117/1.NPh.2.4.045001]

Keywords: spatial frequency domain imaging; tissue optics; LED microprojector; functional activation; scattering; absorption; cerebral metabolic rate of oxygen.

Paper 15013RR received Feb. 27, 2015; accepted for publication Sep. 15, 2015; published online Oct. 12, 2015.

1 Introduction

Alzheimer's disease (AD) is a neurodegenerative disease affecting 35 million people worldwide.[1] There is interest in developing *in vivo* imaging methods to enhance our understanding of the disease and to help facilitate earlier intervention.[2,3] Most AD cases (60% to 90%) are associated with ischemic vascular disease, and 90% of AD patients exhibit cerebral amyloid angiopathy (CAA), a vascular disease caused by amyloid deposition in the vessels.[1] An association between AD and reduced vascular reactivity, a physiological consequence of CAA, was demonstrated with transcranial Doppler,[4–6] functional magnetic resonance imaging (fMRI),[7,8] positron emission tomography (PET),[9] and single-photon emission computed tomography (SPECT)[10] techniques. Neurovascular coupling (NVC), the localized vasodilation that occurs from a specific metabolic demand, is also reduced in AD with visual[11] and verbal fluency[12] challenges. Therefore, accurate development of imaging biomarkers sensitive to vascular reactivity and NVC is of great interest for early detection of AD.

Rodent models of AD are useful for studying the timecourse of pathology. In the triple transgenic APP/PS1/tau (3xTg-AD) mouse model[13] of AD, our previous work demonstrated significant differences in baseline absorption and scattering properties at near-infrared (NIR) wavelengths (650 to 970 nm) as well as magnitude differences in brain oxygenation after inhaled-hyperoxia.[14] The 3xTg-AD mice developed accelerated vascular pathology as toxic amyloid and tau proteins accumulated in the brain.[15] Others observed changes in NVC in a CAA mouse model with laser speckle imaging.[16] NVC primarily has been studied in rats with multispectral imaging, which relies on the modified Beer–Lambert law (MBLL) [Eq. (1)][17,18] to fit oxy- and deoxyhemoglobin (HbO_2 and Hb, respectively) concentration changes, based on reflectance changes at two or more wavelengths of light,

$$\Delta A(\lambda, t) = \sum [E(\lambda) \times \Delta c(t) \times \mathrm{DPF}(\lambda)], \quad (1)$$

where $\Delta A(\lambda, t)$ is the base-10 logarithm of the normalized change in reflectance at wavelength λ and time t, $E(\lambda)$ is the wavelength-dependent extinction coefficient of chromophore c, $\Delta c(t)$ is the change in concentration of chromophore c at time t, and $\mathrm{DPF}(\lambda)$ is the differential pathlength factor defined mathematically as $\Delta A / \delta \mu_a$. The absorption (μ_a) and reduced scattering (μ_s') coefficients used to calculate $\mathrm{DPF}(\lambda)$ are usually assumed *a priori* to be constant values. However, we demonstrated that the baseline optical properties of AD and control mice are significantly different.[14,15,19]

Hence, we postulate that the use of assumed baseline optical properties may lead to errors in calculating changes in

*Address all correspondence to: Bruce J. Tromberg, E-mail: bjtrombe@uci.edu

2329-423X/2015/$25.00 © 2015 SPIE

hemoglobin concentrations, especially when models of cerebrovascular disease are used. The objectives of this study are twofold: (1) to compare hemodynamic response to evoked stimuli in 3xTg-AD and control mice and (2) to compare the evoked responses in mice when using commonly assumed baseline optical properties versus directly measured optical properties in the MBLL calculation. We found the baseline optical properties in both controls and AD mice measured using spatial frequency domain imaging (SFDI) differed from literature-reported optical property values, resulting in significantly different calculations of hemoglobin changes in multispectral imaging of an evoked stimulus response.

2 Methods

2.1 *Animals*

We imaged 20-month-old C57BL/6 mice ($n = 8$) and 3xTg-AD mice ($n = 5$) under 1.2% isoflurane anesthesia in a 21% oxygen/79% nitrogen air mix (Oxydial, Starr Life Sciences Corp.). Isoflurane is a strong vasodilator at higher concentrations (>1.6%),[20] but cortical vasodilatory reserve has been shown to be intact in rodents anesthetized under 1.2% isoflurane.[15,21] After inducing anesthesia, the head of each mouse was secured in a stereotaxic frame (Stoelting Co.), and body temperature was maintained at 37°C with a thermistor-controlled heating pad (CWE, Inc.). We removed the skin above the scalp and thinned the skull within a 3 mm × 3 mm region of interest (ROI) bilaterally over the hindpaw cortical sensory area with a dental drill. A well was created with petroleum jelly around the ROI, filled with sterile saline and covered with a glass coverslip to maintain optical transparency of the thin skull. All procedures were performed in accordance with the regulations of the Institutional Animal Care and Use Committee of the University of California, Irvine (protocol 2010-2934).

2.2 *Spatial Frequency Domain Imaging*

SFDI is a wide-field, camera-based technique capable of measuring absorption (μ_a) and reduced scattering (μ_s') coefficients in tissue on a pixel-by-pixel basis. SFDI works by structuring light into two-dimensional sinusoidal patterns and projecting them onto the tissue surface.[22] The tissue acts as a spatial filter and blurs the structured patterns. By projecting patterns of differing spatial frequencies, the modulation transfer function of the tissue can be found, from which a unique pair of optical absorption and scattering coefficients is determined for each pixel in the ROI.[23]

The flexible LED and modulation element (FLaME) platform used for SFDI and multispectral imaging was described previously[24] and is shown in Fig. 1. We sequentially projected five spatial frequencies (0, 0.05, 0.1, 0.2, and 0.4 mm^{-1}), with each sinusoidal frequency pattern projected three times, at phases of 0, 120, and 240 deg. The remitted reflectance was captured by two cameras (460 and 530 nm, 10-nm FWHM bandpass filters, Thorlabs) and saved for offline processing and analysis. Total acquisition time for 10 repetitions (150 images/camera) was approximately 3 min. Reflectance at each spatial frequency and wavelength was calculated using

$$R_{fx} = (2^{1/2}/3) \times [(I_1 - I_2)^2 + (I_1 - I_3)^2 + (I_2 - I_3)^2]^{1/2}, \quad (2)$$

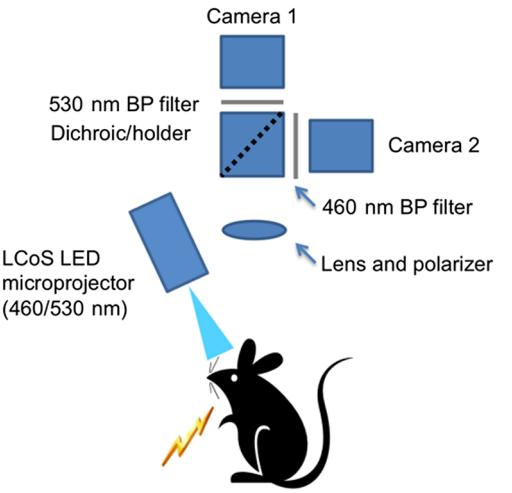

Fig. 1 Diagram of flexible LED and modulation element experimental imaging setup (from Ref. 24). All components were controlled with LabVIEW software on a personal computer.

where R_{fx} is the demodulated frequency amplitude image and I_1, I_2, and I_3 are the three captured images at three different phases, respectively, collected by each camera. R_{fx} images were further calibrated using silicone phantoms having known optical properties to correct for factors inherent in the instrument, such as inhomogeneous light distribution in the imaging plane or lens aberration. A Levenberg–Marquardt algorithm was used to solve for values of μ_a and μ_s' that best matched the frequency-dependent sample reflectance to calculated values from a scaled Monte Carlo model of light transport.[23]

2.3 *Correction Factor for Baseline* μ_a

SFDI relies on a model of light transport that assumes absorbers are homogeneously distributed. However, our sample measurements are of highly absorbing hemoglobin packed into blood vessels in the brain. Given a sufficiently large vessel radius, μ_a can be underestimated due to light not interrogating the whole cross section of a vessel. An established correction factor $C(\lambda)$[25,26] was used to account for this

$$C(\lambda) = \frac{1 - \exp[-2 * \mu_{a,b}(\lambda) * R_{vessel}]}{2 * \mu_{a,b}(\lambda) * R_{vessel}}, \quad (3)$$

where $\mu_{a,b}(\lambda)$ is the average absorption coefficient of whole blood inside blood vessels and R_{vessel} is the average vessel radius in the interrogated volume. We calculated $\mu_{a,b}(\lambda)$ with an estimated hemoglobin oxygen saturation of 50% and a normal concentration of 2062 μM,[27] using 64,500 g/mol as the molecular weight of a hemoglobin tetramer molecule. Mouse cortical capillaries are 4 to 6 μm[28] in diameter and surface vessels are 100 to 400 μm[29] in diameter. Average cortical R_{vessel} was estimated to be 15 μm,[30,31] leading to calculated correction factor values of 0.79 at 460 nm and 0.76 at 530 nm. The uncorrected μ_a was divided by the appropriate correction factor, and this is the value reported in the results and used in all further analyses.

At 460 and 530 nm, the absorption coefficients of cytochrome, lipids, and water are several orders of magnitude smaller than the absorption coefficients for oxyhemoglobin and deoxyhemoglobin.[32–35] With only two wavelengths

measured, we chose to fit for the two dominant absorbers, oxy- and deoxyhemoglobin. Baseline oxy- and deoxyhemoglobin values were calculated from the corrected μ_a values using least-squares linear fit of the Beer–Lambert law as before.[24]

2.4 *Multispectral Imaging of Evoked Stimulus Response*

Following SFDI data acquisition, the FLaME system was used to measure the NVC response to hindpaw stimulation. Light at 460 and 530 nm was continuously projected onto the mouse brain with an AAXA microprojector, and images were acquired at a frame rate of 2 Hz. An experiment consisted of ninety 30-s trials, with each trial consisting of 2 s of baseline followed by 2 s of 10 Hz, 1-ms electrical pulse stimulation, and 26 s of monitored response time. The electrical stimulus was sent through two needle electrodes inserted subcutaneously into the palmar surface of the left hindpaw of a mouse between the first and second digits and the fourth and fifth digits. An isolated stimulator (World Precision Instruments), controlled by TTL pulses sent from a data acquisition board (National Instruments), adjusted the stimulation current needed to elicit a hindpaw twitch (average 1.5 mA). We averaged the ninety 30-s trials in order to determine the average change in reflectance for each mouse.

2.5 *Hemoglobin Change Calculations*

Hemoglobin concentration changes were calculated using the MBLL with both a literature-derived DPF for mouse brain and SFDI-derived DPF. The DPF is a function of μ_a and μ_s' of the sample, and it was solved for using the method previously described.[36] We employed Monte Carlo simulation code[23] assuming uniform illumination, a tissue refractive index of $n = 1.43$, and a scattering anisotropy factor of $g = 0.9$. The DPF estimates from Monte Carlo simulations only require inputs of μ_a and μ_s', which are measured by SFDI with no prior knowledge of possible chromophores and scatterers. To calculate the literature-derived DPF, we used common assumptions of absorption ($\mu_{a,460\ nm} = 0.83\ mm^{-1}$, $\mu_{a,530\ nm} = 0.91\ mm^{-1}$, reflecting 60 μM HbO_2 and 40 μM Hb in the brain) and wavelength-independent scattering ($\mu'_{s\,460\ and\ 530\ nm} = 1.0\ mm^{-1}$) in mice.[37,38] DPF has units of optical density (OD) mm.

2.6 *Data Analysis*

Total hemoglobin (THb) was calculated as the sum of HbO_2 and Hb. Oxygen saturation (O_2 sat) was calculated as $(HbO_2/THb) \times 100$. ROIs were selected manually to include the hindpaw somatosensory cortex contralateral to the side of stimulation [Fig. 2(a)], and ROI pixel values were averaged for each mouse. Further analyses used average ROI values for each mouse, and error bars are standard error between mice in each group. p values were calculated using a Student two-tailed t-test. All analyses were done in MATLAB.[39]

3 Results

3.1 *Baseline SFDI Measurements Compared to Literature-Reported Values*

Absorption contrast was seen between the 3xTg-AD mice and controls at 460 and 530 nm [Table 1 and Fig. 2(b)]. Compared to assumed values in the literature, measured mean μ_a values for control and 3xTg-AD mice at 460 nm were 1.2% and 22% lower, respectively; at 530 nm, they were 22% and 40% lower than assumed values. Moreover, mean absorption values differed significantly between control and 3xTg-AD mice at 460 and 530 nm. A wavelength-dependent linear least-squares fit of μ_a values to the Beer–Lambert law allowed us to calculate HbO_2, Hb, THb, and O_2 sat for control versus 3xTg-AD mice [Table 2 and Fig. 3(b)]. These results of lower THb and HbO_2 in the 3xTg-AD mice are in agreement with our previous measurements using NIR wavelengths.[14,15] This likely reflects decreased blood vessel density and volume in 3xTg-AD mice

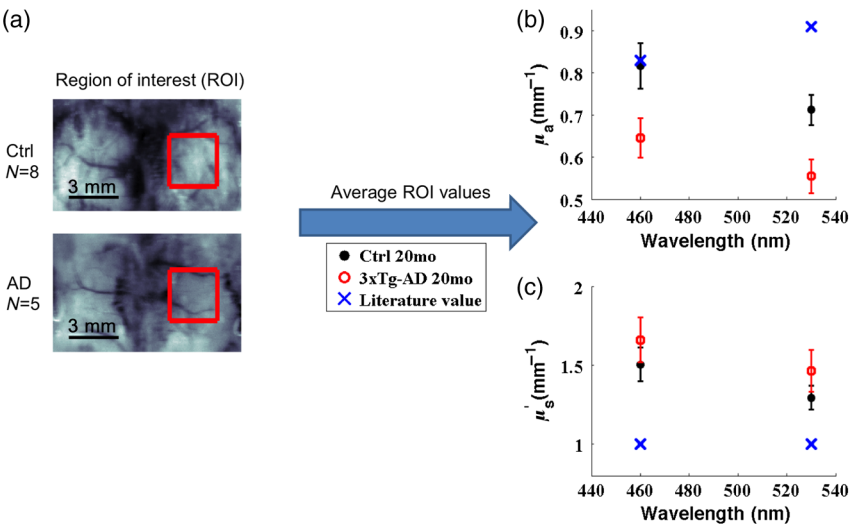

Fig. 2 Spatial frequency domain imaging (SFDI)-measured μ_a and μ_s' are different from literature-reported values at 460 and 530 nm. (a) A region of interest (ROI, red square) was selected over the contralateral somatosensory cortex of the stimulated hindlimb. (b) The average and standard error of ROI values in each group are shown for μ_a and compared to a literature-reported value.[37] (c) The average and standard error of ROI values in each group are shown for μ_s' and compared to a typically assumed literature-reported value of 1 mm^{-1}.[38]

Table 1 Comparison of baseline optical properties and differential pathlength factor (DPF) for control and 3xTg-AD mice.

	Control	3xTg-AD	*p* value
μ_a (460 nm)	0.82 ± 0.05 mm^{-1}	0.65 ± 0.05 mm^{-1}	0.04
μ_a (530 nm)	0.71 ± 0.04 mm^{-1}	0.55 ± 0.04 mm^{-1}	0.02
μ_s' (460 nm)	1.5 ± 0.1 mm^{-1}	1.7 ± 0.1 mm^{-1}	0.21
μ_s' (530 nm)	1.3 ± 0.1 mm^{-1}	1.5 ± 0.1 mm^{-1}	0.21
DPF (460 nm)	$0.5813 \pm$ 0.0408 OD mm	$0.6358 \pm$ 0.0365 OD mm	0.38
DPF (530 nm)	$0.6562 \pm$ 0.0327 OD mm	$0.7293 \pm$ 0.0455 OD mm	0.21

Table 2 Comparison of baseline hemoglobin fits for control and 3xTg-AD mice.

	Control	3xTg-AD	*p* value
HbO_2	77 ± 7 μM	60 ± 4 μM	0.10
Hb	8 ± 4 μM	2 ± 1 μM	0.27
THb	85 ± 4 μM	62 ± 5 μM	0.004
O_2 sat	$90 \pm 5\%$	$96 \pm 2\%$	0.38

compared to age-matched control mice, as we have shown previously.[15]

Compared to controls, μ_s' averaged 14% higher in the 3xTg-AD mice, but the difference was not significant [Table 1 and Fig. 2(c)]. SFDI-derived DPF was calculated from the μ_a and μ_s' maps using Monte Carlo simulations. For control and 3xTg-AD mice, mean DPF values at 460 nm were 8.7% and 0.14% lower, respectively, than the literature-derived DPF (0.6367 OD mm); at 530 nm, they were 3.7% and 9.7% higher, respectively, than the literature-calculated value (0.6328 OD mm) (Table 1). In the 3xTg-AD mice, the decrease in μ_a and increase in μ_s' compared to controls have opposing effects on DPF such that the difference in DPF values was statistically insignificant between 3xTg-AD mice and controls.

3.2 *Qualitative Difference in Blood Overperfusion Between 3xTg-AD and Control Mice*

Before a quantitative MBLL calculation of hemoglobin change was performed, the normalized reflectance change in the two wavelengths was averaged across all 30-s trials. Increased blood flow from brain activation could be seen in the ROIs with 530-nm reflectance, since that is an isosbestic point for HbO_2 and Hb absorption (Fig. 4). The overperfusion response lasted longer in the controls compared to 3xTg-AD mice. Interestingly, an overperfusion response to activation was seen bilaterally and diffusely, differing from the more localized response seen in rats.[40] Others have seen localized responses in mice with whisker stimulation.[41] However, another group has also observed a bilateral diffuse response to hindpaw stimulation,[42] and it may be due to bilateral activation of pain pathways to the thalami with a larger stimulus.[43]

3.3 *Effect of Calculating Hemoglobin Concentration Changes Using the MBLL with SFDI-Derived Versus Literature-Derived DPFs*

The hemodynamic changes resulting from the MBLL equation can be seen as group average tracings in Fig. 5, either with the SFDI-derived DPF [Figs. 5(a) and 5(b)] or the literature-reported DPF [Figs. 5(c) and 5(d)]. The time course of the vascular response in control mice agreed with previous studies in mice.[42,44] Interestingly, previous multispectral imaging of forepaw stimulation in mice showed an increase in Hb and THb with a decrease in HbO_2,[44] but our hindpaw stimulation results show an increase in HbO_2 and THb with a decrease in Hb, agreeing with studies in rats and most functional activation studies.[40,44,45]

In control mice, hemodynamic changes calculated from the MBLL using the SFDI-derived DPFs show a 38% increase in peak HbO_2 and threefold decrease in Hb changes compared to calculations using assumed DPFs [Figs. 6(a) and 6(d)]. Most notably, the overall change in Hb during the overperfusion (i.e., area-under-the-curve from 4 to 30 s) was calculated as a slight increase with assumed DPFs, as opposed to the expected decrease with SFDI-derived DPFs (4 ± 7 μMs versus -23 ± 5 μMs, $p < 0.0001$) [Figs. 6(b) and 6(e)]. These differences

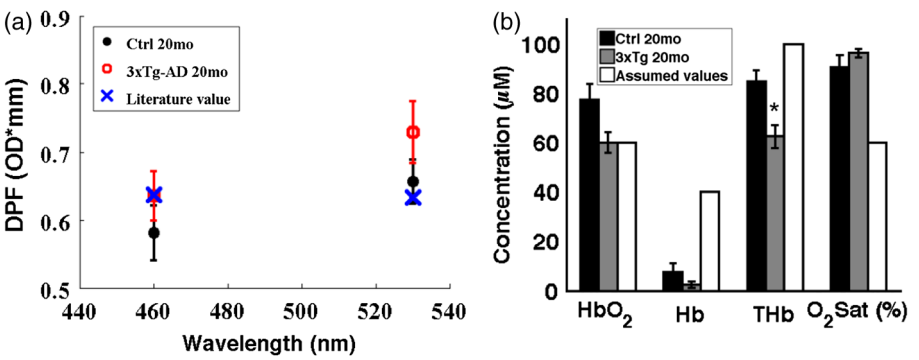

Fig. 3 (a) The average and standard error of ROI values in each group are shown for differential pathlength factor (DPF) and compared to a literature-reported value.[36] (b) The average and standard error of HbO_2, Hb, THb, and O_2 sat in each group are shown and compared to typically literature-reported values.[37,38]

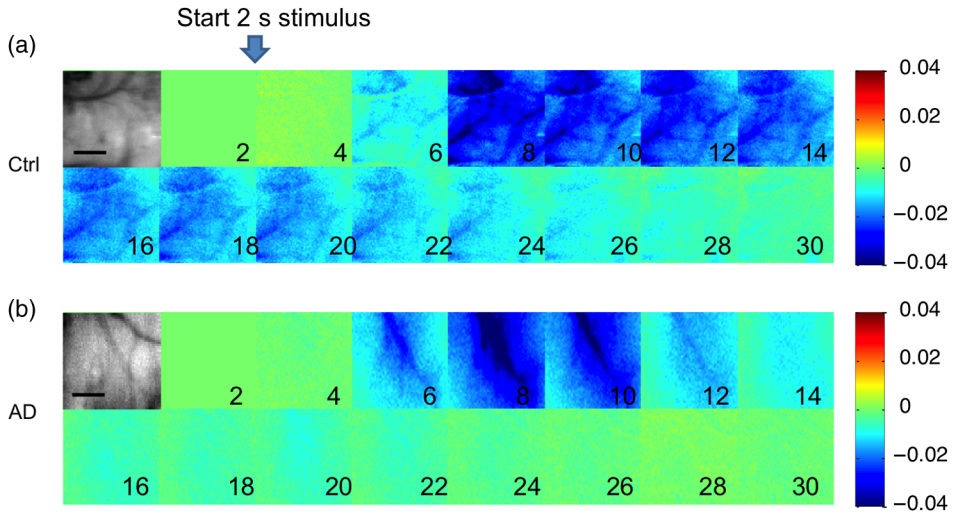

Fig. 4 Representative montage of the normalized reflectance change at 530 nm in the ROI (grayscale image) for (a) controls and (b) 3xTg-AD mice. Stimulation started after 2 s of baseline, lasted for 2 s, and images every 2 s subsequently are shown up to 30 s. Color scale shows normalized changes from −4% to 4%. Scale bars (grayscale images) are 1 mm.

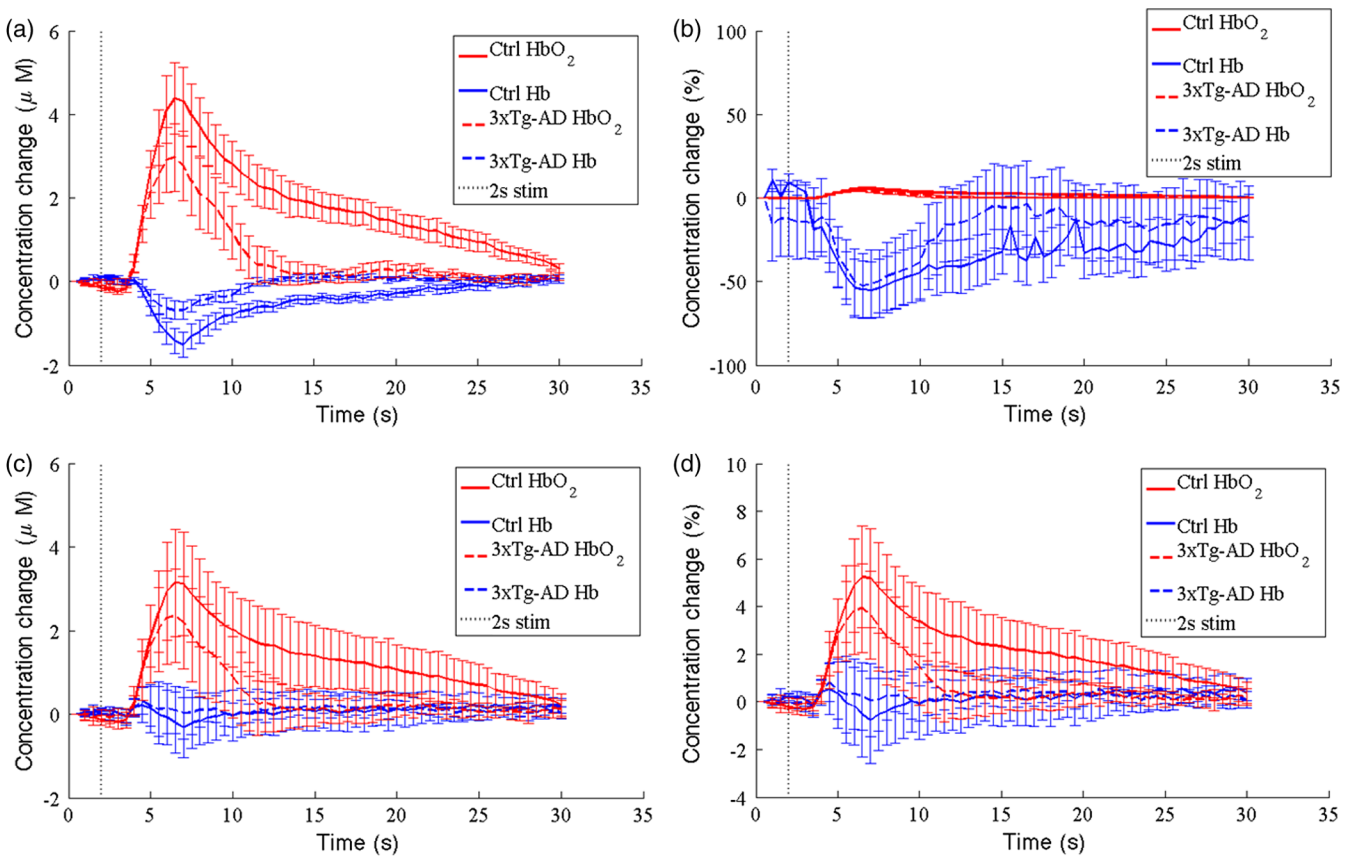

Fig. 5 Average tracings of HbO_2 (red lines) and Hb (blue lines) changes in controls (solid lines) and 3xTg-AD mice (dotted lines). Stimulation occurred from 2 to 4 s (shaded area) and standard error bars are shown. (a) Absolute hemoglobin changes calculated from the MBLL using SFDI-measured baseline optical properties. (b) Percentage hemoglobin changes calculated from the MBLL using SFDI-measured baseline optical properties. (c) Absolute hemoglobin changes calculated from the MBLL using literature-reported baseline optical properties. (d) Percentage hemoglobin changes calculated from the MBLL using literature-reported baseline optical properties.

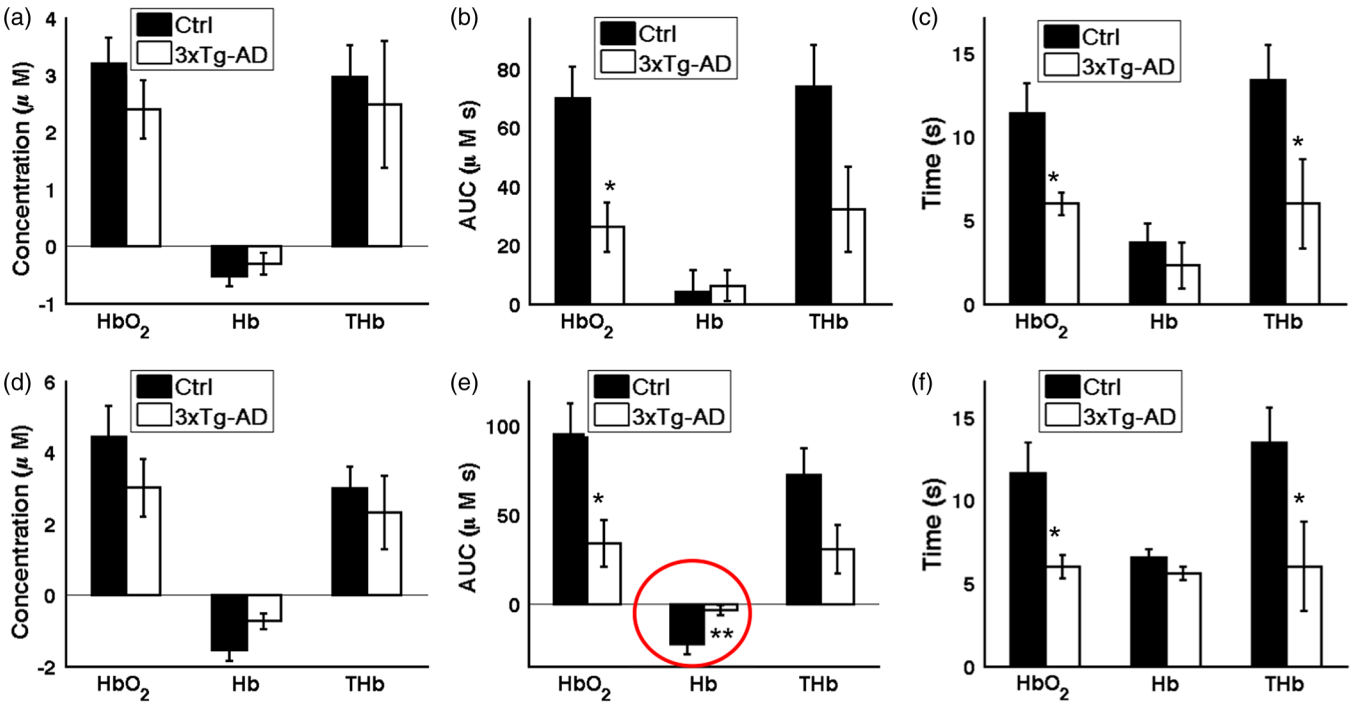

Fig. 6 Three parameters are compared that describe the overperfusion response in the mice. Graphs in (a), (b), and (c) are calculated in the case where the MBLL was informed with assumed DPFs, based on optical property values commonly used by other groups. Graphs in (d), (e), and (f) are calculated in the case where the MBLL was informed with SFDI-derived DPFs. (a, d) Peak hemodynamic change was determined by finding the largest concentration change from baseline of HbO_2, Hb, and THb after the 2-s stimulation. (b, e) Area-under-the-curve (AUC) of the overperfusion after the 2-s stimulation was calculated by integrating the average hemoglobin concentration changes from 4 to 30 s. (c, f) Relaxation time T_{50} of the hemodynamic response was calculated as the time the overperfusion returns to half its peak value. *$p < 0.05$ for both assumed DPF baseline and SFDI-derived DPF baseline for hemodynamic fitting. **$p < 0.05$ for SFDI-derived DPF baseline and not assumed DPF baseline.

suggest deriving DPFs from actual optical property baselines has a large impact on the calculated hemoglobin change.

By comparing control to 3xTg-AD mice with SFDI-derived DPFs for the MBLL calculations, we saw a threefold larger and twofold longer period of overperfusion with HbO_2 [Figs. 6(e) and 6(f)]. Furthermore, SFDI correction of the DPF revealed a sevenfold larger reduction in Hb washout in controls compared to AD mice [Fig. 6(e)]. This reduction would have been masked had assumed DPF values been used [Fig. 6(b)]. This is the first study, to our knowledge, showing hemodynamic response in a mouse model of AD to evoked stimuli, and these results support the hypothesis that a diminished hemodynamic response to a metabolic demand is part of the pathogenesis of AD.

4 Discussion

This is the first measurement of baseline optical properties in an AD mouse model and age-matched controls to inform the MBLL during an evoked stimulus experiment. We found that the baseline optical properties probed by visible wavelengths (460 nm, 530 nm) substantially differ from previously published values of μ_a and μ_s'.[37,38,40] Most notably, the mean baseline cortical oxygen saturation was 90% and 96% for control and 3xTg-AD mice, respectively. Previously published work in the same mouse model, when using an NIR-SFDI instrument, found baseline HbO_2 and Hb for 20-month-old control mice were 77 and 58 μM, respectively (oxygen saturation 57%); baseline HbO_2 and Hb for 20-month-old 3xTg-AD mice were 58 and 49 μM, respectively (oxygen saturation 54%).[15]

This implies that either the visible-SFDI-measured saturations are inaccurate or we are accurately measuring superficial cortical oxygen saturations, which differ from deep cortical saturations interrogated with NIR. Anatomically, highly oxygenated superficial arterioles dive deep into the cortex. Other investigators have found partial pressure of oxygen to be 50 mm Hg up to a depth of 250 μm into the cortex, and it decreases with depth in the mouse brain.[46,47] It has also been shown under normal imaging conditions that the cortex can be up to 10°C lower than body temperature,[48] potentially left-shifting the hemoglobin oxygen-dissociation curve of a mouse[49] to account for 90% O_2 sat. Future experiments should monitor and control blood gas, heart rate/cardiac output, and brain surface temperature to better validate these results. Multilayer heterogeneous light tissue transport modeling combined with fMRI could also inform and validate these preliminary results.[50]

One possible source of error is the μ_a correction factor, $C(\lambda)$. $C(\lambda)$ of NIR measurements is effectively 1 since the μ_a of whole blood in the NIR is 100-fold lower than in the visible. However, at the hemoglobin isosbestic point 530 nm, C (530 nm) can range from 0.96 to 0.13 for an average vessel radius of 2 to 200 μm, respectively. Therefore, the total hemoglobin measurements depend on the average vessel radius, which are not measured or known in our mouse model. C (460 nm) could also potentially affect the baseline oxygen saturation estimation.

In *post-hoc* analysis, sweeping the assumed average vessel radius (15 to 150 μm) and average oxygen saturation (30 to 100%) of whole blood did not correct the SFDI-measured raw μ_a values to match literature-reported oxygen saturations with appropriate total hemoglobin concentrations. Large differences in cytochrome and lipid concentration could also alter the baseline hemoglobin concentration and saturation calculations. Cytochrome oxidase activity is reduced as much as 26% and 50% in human postmortem AD brain tissue[51] and platelets,[52] respectively. Future experiments that use multiple (>3) wavelengths to fit for additional chromophores could potentially address this issue.

Wavelength-dependent scattering measured with visible-SFDI was also attenuated when compared to NIR-SFDI measurements.[15] Reduced scattering coefficients ranged from approximately 1.6 to 1 mm^{-1} from 650 to 970 nm, respectively. In the NIR, wavelength-dependent scattering was significantly higher in 3xTg-AD brains compared to controls, which could be attributed to morphological changes caused by an increased inflammatory state.[19] We hypothesize the plateauing of μ_s' at 460 and 530 nm may be partially explained by the limited penetration depth of visible wavelengths versus NIR wavelengths[53] and the layered nature of the mouse skull and brain. *Ex vivo* from 460 to 530 nm, the brain is highly scattering ($\mu_s' \sim 6$ mm^{-1})[54] while the skull ($\mu_s' \sim 3.5$ mm^{-1}) and CSF are less so.[55,56] In the visible wavelength regime, the thinned skull and underlying cerebral spinal fluid take up a higher partial volume fraction, diluting the perceived scattering from the brain. Differences in thin skull preparation, as well as the effect of saline on the skull,[24] could also account for the variability in μ_s' measured with visible-SFDI, ameliorating the difference between control and 3xTg-AD brains seen with NIR-SFDI.

The percentage change line graphs in Figs. 5(b) and 5(d) highlight a major difference in how we would interpret the underlying biology of the optical signals. Such high baseline oxygen saturation would significantly affect a calculation often used to approximate relative change in brain metabolism during an evoked stimulus response, the relative change in cerebral metabolic rate of oxygen ($rCMRO_2$) [Eqs. (4) and (5)]:[37,38]

$$\gamma = \frac{\Delta \mathrm{HbT}\nu}{\mathrm{HbT}\nu^{o}} \Big/ \frac{\Delta \mathrm{HbT}}{\mathrm{HbT}^{o}}, \tag{4}$$

$$1+\mathrm{rCMRO_2} = \left(1+\frac{\Delta \mathrm{CBF}}{\mathrm{CBF}^{o}}\right)\left(1+\frac{\Delta \mathrm{Hb}}{\mathrm{Hb}^{o}}\right)\left(1+\frac{\gamma \Delta \mathrm{HbT}}{\mathrm{HbT}^{o}}\right)^{-1}, \tag{5}$$

where $rCMRO_2$ is equal to the fractional change in cerebral blood flow (CBF) (typically measured with laser speckle imaging) multiplied by the fractional change in Hb and divided by the fractional change in THb in the veins. Specifically, in our measured evoked stimulus response, the fractional decrease in Hb (e.g., −50%) would overwhelm the smaller fractional increase in CBF (e.g., typically +10%) and produce a negative change in local metabolism. It is unclear how to integrate these baseline oxygen saturation measurements into the $rCMRO_2$ calculation, but this hypothetical scenario underscores the importance of accurate knowledge of baseline conditions to interpret multispectral imaging results.

In our evoked stimulus experiment, relatively large signals such as the HbO_2 overperfusion were qualitatively the same regardless of using assumed or SFDI-informed DPFs. We replicated the attenuated overperfusion response that has been well characterized with laser speckle imaging in a CAA mouse model,[16] NIR spectroscopy measurements in AD patients,[11,12] and fMRI blood-oxygen-level dependent (BOLD) response in a rat model of AD.[57] The fMRI BOLD response has also been shown to be sensitive to loss of clinically significant tasks in patients with AD, such as face recognition[58] and stepwise loss of smell with worsening AD.[59] However, task-based fMRI BOLD signal interpretation is limited by fluctuations in the baseline perfusion and metabolic states of the brain.[60,61] Our work in characterizing the 3xTg-AD baseline optical properties indicates that there are global and spatial differences in oxygen saturation compared to control brains. Knowledge of the baseline optical properties allowed detection of Hb washout differences during an evoked stimulus in 3xTg-AD mice. In the context of early detection of AD, our work supports the use of resting state fMRI, arterial spin labeling, and PET/SPECT to fully characterize baseline perfusion and metabolism differences in AD that may then further inform task-based fMRI BOLD signals.

In conclusion, this work emphasizes the differences in baseline optical properties from typically assumed values when studying metabolism in rodents with varying thin skull thicknesses, comparing disease models of AD, and using visible versus NIR wavelengths in multispectral imaging. We have shown that SFDI-derived DPF allows for more accurate determination of hemodynamic response to an evoked stimulus in an AD mouse model.

Acknowledgments

Funding for this work was supported in part by the NIH (NIBIB) Laser Microbeam and Medical Program (P41EB015890), NIH (NIBIB) Grant (R21 EB014440), NIH (NINDS) Grant (R21 NS078634), NIH (NIA) Grant (R01 A6-21982), NIH (NIA) Ruth Kirschstein NRSA fellowship (5F30AG039949-02), U.C. Irvine MSTP, and the Arnold and Mabel Beckman Foundation.

References

1. H. W. Querfurth and F. M. LaFerla, "Alzheimer's disease," *N. Engl. J. Med.* **362**(4), 329–344 (2010).
2. W. E. Klunk et al., "Imaging brain amyloid in Alzheimer's disease with Pittsburgh compound-B," *Ann. Neurol.* **55**(3), 306–319 (2004).
3. J. L. Price et al., "Neuropathology of nondemented aging: presumptive evidence for preclinical Alzheimer disease," *Neurobiol. Aging* **30**(7), 1026–1036 (2009).
4. E. Vicenzini et al., "Cerebrovascular reactivity in degenerative and vascular dementia: a transcranial Doppler study," *Eur. Neurol.* **58**(2), 84–89 (2007).
5. M. Silvestrini et al., "Cerebrovascular reactivity and cognitive decline in patients with Alzheimer disease," *Stroke* **37**(4), 1010–1015 (2006).
6. A. Stefani et al., "CSF biomarkers, impairment of cerebral hemodynamics and degree of cognitive decline in Alzheimer's and mixed dementia," *J. Neurol. Sci.* **283**(1–2), 109–115 (2009).
7. U. S. Yezhuvath et al., "Forebrain-dominant deficit in cerebrovascular reactivity in Alzheimer's disease," *Neurobiol. Aging* **33**(1), 75–82 (2012).
8. A. Kassner et al., "Blood-oxygen level dependent MRI measures of cerebrovascular reactivity using a controlled respiratory challenge: reproducibility and gender differences," *J. Magn. Reson. Imaging* **31**(2), 298–304 (2010).
9. G. Stoppe et al., "Cerebrovascular reactivity to acetazolamide in (senile) dementia of Alzheimer's type: relationship to disease severity," *Dementia* **6**(2), 73–82 (1995).
10. L. Pavics et al., "rCBF SPECT and the acetazolamide test in the evaluation of dementia," *Nucl. Med. Rev. Cent. East Eur.* **1**(1), 13–19 (1998).

11. J. B. Zeller et al., "Altered parietal brain oxygenation in Alzheimer's disease as assessed with near-infrared spectroscopy," *Am. J. Geriatr. Psychiatry* **18**(5), 433–441 (2010).
12. M. J. Herrmann et al., "Reduced prefrontal oxygenation in Alzheimer disease during verbal fluency tasks," *Am. J. Geriatr. Psychiatry* **16**(2), 125–135 (2008).
13. S. Oddo et al., "Triple-transgenic model of Alzheimer's disease with plaques and tangles: intracellular Abeta and synaptic dysfunction," *Neuron* **39**(3), 409–421 (2003).
14. A. J. Lin et al., "Spatial frequency domain imaging of intrinsic optical property contrast in a mouse model of Alzheimer's disease," *Ann. Biomed. Eng.* **39**(4), 1349–1357 (2011).
15. A. J. Lin et al., "Optical imaging in an Alzheimer's mouse model reveals amyloid-dependent vascular impairment," *Neurophotonics* **1**(1), 011005 (2014).
16. H. K. Shin et al., "Age-dependent cerebrovascular dysfunction in a transgenic mouse model of cerebral amyloid angiopathy," *Brain* **130**(9), 2310–2319 (2007).
17. D. T. Delpy et al., "Estimation of optical pathlength through tissue from direct time of flight measurement," *Phys. Med. Biol.* **33**(12), 1433–1442 (1988).
18. A. K. Dunn et al., "Simultaneous imaging of total cerebral hemoglobin concentration, oxygenation, and blood flow during functional activation," *Opt. Lett.* **28**(1), 28–30 (2003).
19. A. J. Lin et al., "In vivo optical signatures of neuronal death in a mouse model of Alzheimer's disease," *Lasers Surg. Med.* **46**(1), 27–33 (2014).
20. E. I. Eger, "The pharmacology of isoflurane," *Br. J. Anaesth.* **56**(Suppl. 1), 71S–99S (1984).
21. M. A. Franceschini et al., "The effect of different anesthetics on neurovascular coupling," *Neuroimage* **51**(4), 1367–1377 (2010).
22. D. J. Cuccia et al., "Modulated imaging: quantitative analysis and tomography of turbid media in the spatial-frequency domain," *Opt. Lett.* **30**(11), 1354–1356 (2005).
23. D. J. Cuccia et al., "Quantitation and mapping of tissue optical properties using modulated imaging," *J. Biomed. Opt.* **14**(2), 024012 (2009).
24. A. J. Lin et al., "Visible spatial frequency domain imaging with a digital light microprojector," *J. Biomed. Opt.* **18**(9), 096007 (2013).
25. L. O. Svaasand et al., "Therapeutic response during pulsed laser treatment of port wine stain: dependence on vessel diameter and depth in dermis," *Lasers Med. Sci.* **10**, 235–243 (1995).
26. R. L. van Veen, W. Verkruysse, and H. J. Sterenborg, "Diffuse-reflectance spectroscopy from 500 to 1060 nm by correction for inhomogeneously distributed absorbers," *Opt. Lett.* **27**(4), 246–248 (2002).
27. E. S. Russell, E. F. Neufeld, and C. T. Higgins, "Comparison of normal blood picture of young adults from 18 inbred strains of mice," *Proc. Soc. Exp. Biol. Med.* **78**(3), 761–766 (1951).
28. E. P. Meyer et al., "Altered morphology and 3D architecture of brain vasculature in a mouse model for Alzheimer's disease," *Proc. Natl. Acad. Sci. U. S. A.* **105**(9), 3587–3592 (2008).
29. W. Lu et al., "Photoacoustic imaging of living mouse brain vasculature using hollow gold nanospheres," *Biomaterials* **31**(9), 2617–2626 (2010).
30. A. P. Pathak et al., "Three-dimensional imaging of the mouse neurovasculature with magnetic resonance microscopy," *PLoS One* **6**(7), e22643 (2011).
31. Y. Sekiguchi et al., "Measuring the vascular diameter of brain surface and parenchymal arteries in awake mouse," *Adv. Exp. Med. Biol.* **789**, 419–425 (2013).
32. S. Prahl, "Tabulated molar extinction coefficient for hemoglobin in water," http://omlc.org/spectra/hemoglobin/summary.html (17 May 2015).
33. R. M. Pope and E. S. Fry, "Absorption spectrum (380–700 nm) of pure water. II. Integrating cavity measurements," *Appl. Opt.* **36**(33), 8710–8723 (1997).
34. M. Cope, *The Application of Near Infrared Spectroscopy to Non Invasive Monitoring of Cerebral Oxygenation in the Newborn Infant*, Department of Medical Physics and Bioengineering, University College London, London, England (1991).
35. R. L. van Veen et al., "Determination of visible near-IR absorption coefficients of mammalian fat using time- and spatially resolved diffuse reflectance and transmission spectroscopy," *J. Biomed. Opt.* **10**(5), 054004 (2005).
36. M. Kohl et al., "Physical model for the spectroscopic analysis of cortical intrinsic optical signals," *Phys. Med. Biol.* **45**(12), 3749–3764 (2000).
37. A. K. Dunn et al., "Spatial extent of oxygen metabolism and hemodynamic changes during functional activation of the rat somatosensory cortex," *Neuroimage* **27**(2), 279–290 (2005).
38. M. Jones, J. Berwick, and J. Mayhew, "Changes in blood flow, oxygenation, and volume following extended stimulation of rodent barrel cortex," *Neuroimage* **15**(3), 474–487 (2002).
39. The MathWorks Inc., *MATLAB and Statistics Toolbox Release*, The MathWorks, Inc., Natick, Massachusetts (2007).
40. A. Devor et al., "Stimulus-induced changes in blood flow and 2-deoxyglucose uptake dissociate in ipsilateral somatosensory cortex," *J. Neurosci.* **28**(53), 14347–14357 (2008).
41. J. P. Erinjeri and T. A. Woolsey, "Spatial integration of vascular changes with neural activity in mouse cortex," *J. Cereb. Blood Flow Metab.* **22**(3), 353–360 (2002).
42. S. C. Bosshard et al., "Assessment of brain responses to innocuous and noxious electrical forepaw stimulation in mice using BOLD fMRI," *Pain* **151**(3), 655–663 (2010).
43. R. Peyron, B. Laurent, and L. Garcia-Larrea, "Functional imaging of brain responses to pain: a review and meta-analysis (2000)," *Neurophysiol. Clin.* **30**(5), 263–288 (2000).
44. N. Prakash et al., "Temporal profiles and 2-dimensional oxy-, deoxy-, and total-hemoglobin somatosensory maps in rat versus mouse cortex," *Neuroimage* **37**(Suppl. 1), S27–S36 (2007).
45. A. Devor et al., "Frontiers in optical imaging of cerebral blood flow and metabolism," *J. Cereb. Blood Flow Metab.* **32**(7), 1259–1276 (2012).
46. S. Sakadzic et al., "Cerebral blood oxygenation measurement based on oxygen-dependent quenching of phosphorescence," *J. Vis. Exp.* 51, e1694 (2011).
47. M. A. Yaseen et al., "Microvascular oxygen tension and flow measurements in rodent cerebral cortex during baseline conditions and functional activation," *J. Cereb. Blood Flow Metab.* **31**(4), 1051–1063 (2011).
48. A. S. Kalmbach and J. Waters, "Brain surface temperature under a craniotomy," *J. Neurophysiol.* **108**(11), 3138–3146 (2012).
49. L. H. Gray and J. M. Steadman, "Determination of the oxyhaemoglobin dissociation curves for mouse and rat blood," *J. Physiol.* **175**, 161–171 (1964).
50. A. J. Kennerley et al., "Refinement of optical imaging spectroscopy algorithms using concurrent BOLD and CBV fMRI," *Neuroimage* **47**(4), 1608–1619 (2009).
51. S. J. Kish et al., "Brain cytochrome oxidase in Alzheimer's disease," *J. Neurochem.* **59**(2), 776–779 (1992).
52. W. D. Parker, Jr., C. M. Filley, and J. K. Parks, "Cytochrome oxidase deficiency in Alzheimer's disease," *Neurology* **40**(8), 1302–1303 (1990).
53. R. B. Saager et al., "Method for depth-resolved quantitation of optical properties in layered media using spatially modulated quantitative spectroscopy," *J. Biomed. Opt.* **16**(7), 077002 (2011).
54. H. J. C. M. Sterenborg et al., "The spectral dependence of the optical properties of human brain," *Lasers Med. Sci.* **4**(4), 221–227 (1989).
55. M. Firbank et al., "Measurement of the optical properties of the skull in the wavelength range 650–950 nm," *Phys. Med. Biol.* **38**(4), 503–510 (1993).
56. A. Custo et al., "Effective scattering coefficient of the cerebral spinal fluid in adult head models for diffuse optical imaging," *Appl. Opt.* **45**(19), 4747–4755 (2006).
57. B. G. Sanganahalli et al., "Functional MRI and neural responses in a rat model of Alzheimer's disease," *Neuroimage* **79**, 404–411 (2013).
58. A. S. Fleisher et al., "Cerebral perfusion and oxygenation differences in Alzheimer's disease risk," *Neurobiol. Aging* **30**(11), 1737–1748 (2009).
59. J. Wang et al., "Olfactory deficit detected by fMRI in early Alzheimer's disease," *Brain Res.* **1357**, 184–194 (2010).
60. P. Liang et al., "Altered amplitude of low-frequency fluctuations in early and late mild cognitive impairment and Alzheimer's disease," *Curr. Alzheimer Res.* **11**(4), 389–398 (2014).
61. A. S. Fleisher et al., "Resting-state BOLD networks versus task-associated functional MRI for distinguishing Alzheimer's disease risk groups," *Neuroimage* **47**(4), 1678–1690 (2009).

Alexander J. Lin is a graduate of the Medical Scientist Training Program at the University of California, Irvine (UCI). He received his PhD from the Department of Biomedical Engineering at UCI

in 2013, working in the lab of Bruce Tromberg at the Beckman Laser Institute. He plans to continue his residency training in radiation oncology at Washington University in St. Louis.

Adrien Ponticorvo is a project scientist at the Beckman Laser Institute at UCI. His research is focused on the development and application of novel optical imaging techniques to quantify physiology. He holds a PhD in biomedical engineering from the University of Texas at Austin with an emphasis on biomedical optics.

Anthony J. Durkin is an associate professor at the Beckman Laser Institute at UCI. His research is focused on the development and application of optical spectroscopic and quantitative wide-field imaging techniques to characterize superficial tissues *in vivo*. He is codirector of the wide-field functional imaging program at BLI. He holds a PhD in biomedical engineering from the University of Texas at Austin with emphasis on biomedical optics and spectroscopy.

Vasan Venugopalan is a professor and chair of the Department of Chemical Engineering and Materials Science at UCI, with a joint appointment at Beckman Laser Institute. He received a BS degree from the University of California, Berkeley and a ScD degree from Massachusetts Institute of Technology, both in mechanical engineering. His current research is in the areas of computational biophotonics and the interaction of pulsed laser microbeams with cells and tissues.

Bernard Choi is an associate professor of biomedical engineering and surgery at UCI, with appointments at Beckman Laser Institute and Medical Clinic, Edwards Lifesciences Center for Advanced Cardiovascular Technology, and the Children's Hospital of Orange County. His current research is in the field of vascular biophotonics, with current emphases in optical hemodynamic monitoring, microvascular dynamics of tissue in normal and proliferative states, and optical clearing.

Bruce J. Tromberg is the director of the Beckman Laser Institute and Medical Clinic at UCI and principal investigator of the Laser Microbeam and Medical Program (LAMMP), an NIH P41 National Biomedical Technology Center in the BLI. He is a professor with joint appointments in the Departments of Biomedical Engineering and Surgery and has been a member of UCI faculty since 1990.